Journal of The Electrochemical Society

Single-Crystalline $LiNiO_2$ as High-Capacity Cathode Active Material for Solid-State Lithium-Ion Batteries

To cite this article: Raffael Rueß *et al* 2023 *J. Electrochem. Soc.* **170** 020533

Journal of The Electrochemical Society, 2023 **170** 020533

Single-Crystalline $LiNiO_2$ as High-Capacity Cathode Active Material for Solid-State Lithium-Ion Batteries

Raffael Rueß,[1] Davide Gomboso,[1] Mark Ulherr,[1] Enrico Trevisanello,[1] Yuan Ma,[2] Aleksandr Kondrakov,[3] Torsten Brezesinski,[2] and Jürgen Janek[1,2,z]

[1] *Institute of Physical Chemistry and Center for Materials Research, Justus-Liebig-University Giessen (JLU), 35392 Giessen, Germany*
[2] *Battery and Electrochemistry Laboratory (BELLA), Institute of Nanotechnology, Karlsruhe Institute of Technology (KIT), 76344 Eggenstein-Leopoldshafen, Germany*
[3] *BASF SE, 67056 Ludwigshafen am Rhein, Germany*

To increase the specific capacity of $LiNi_{1-x-y}Co_xMn_yO_2$ (NCM) cathode active materials, academia and industry are aiming at a higher nickel content. The end member of this family, $LiNiO_2$ (LNO), offers the highest practical specific capacity, but suffers from morphological and structural instabilities during electrochemical cycling. Especially for the successful implementation in solid-state batteries, coarse-grain powders of single-crystalline LNO need to be synthesized to achieve high performance cells. While NCM-type solid solutions with Co and Mn show sufficient structural stability during synthesis, LNO rapidly decomposes under the conventional conditions for the preparation of single crystals. We address this issue by presenting an alternative route towards single-crystalline LNO based on a flux-assisted synthesis. First, LNO is prepared from NiO and LiOH precursors, which yields agglomerated crystals of LNO with notable Li deficiency. Secondly, this raw LNO is transferred into a Li_2CO_3 melt, which induces crystal growth and separation, and further offers a high chemical potential of Li_2O for defect healing. With this method, well-separated and near-stoichiometric, large-grain LNO single crystals are obtained. When tested in solid-state battery cells, this material yields specific discharge capacities q_{dis} >200 mAh g^{-1} at room temperature and clearly outperforms the state-of-the-art polycrystalline LNO.
 [DOI: 10.1149/1945-7111/acbc4f]

Manuscript submitted December 7, 2022; revised manuscript received February 7, 2023. Published February 28, 2023.

Supplementary material for this article is available online

Today's lithium-ion batteries (LIBs) rely on a liquid electrolyte to shuttle Li^+ ions between anode and cathode. The commonly used electrolytes are flammable and, in extreme cases of battery failure, lead to thermal runaway.[1] For large-scale application of LIBs, e. g. in electric vehicles, such safety issues need to be overcome. One promising concept is the transition towards non-flammable and rigid solid electrolytes that promise significantly improved safety and also enable new cell concepts, such as cells with lithium metal anodes.[1,2] Solid-state batteries (SSBs) use the same cathode active materials (CAMs) as conventional LIBs, mostly high-capacity Ni-rich $LiNi_{1-x-y}Co_xMn_yO_2$ (NCM). However, for a successful implementation of NCM CAMs in SSBs, the conventional polycrystalline particles (secondary particle size >10 μm) appear to be detrimental, as the cracks and gaps between the individual primary particles cannot be filled with the rigid solid electrolyte, causing a large impedance among other effects.[3–5] For SSBs, the use of few μm-sized, separated, single-crystalline NCM will be advantageous, as shown and discussed in previous studies.[5–10]

Single-crystalline NCM has been introduced not only for the application in SSBs, but most prominently to overcome stability issues of high-performance CAMs.[11–14] Improving the energy density of NCM-based cells is commonly pursued by increasing the nickel content which, however, comes at the expense of deteriorated morphological and structural stability.[13] On the one hand, Ni-rich NCM CAMs release reactive oxygen at high states of charge and on the other hand, Ni-rich NCM particles tend to crack under the strain induced by volume changes during (de)lithiation.[15–18] The latter leads to an increase in active surface area which further accelerates the irreversible oxygen release and other side reactions such as transition-metal dissolution.[16,19] Single-crystalline NCM has been introduced to offer better morphological robustness at the expense of lower initial capacity and rate performance. As a result, single-crystalline Ni-rich NCM has been demonstrated to cycle stably for thousands of charge-discharge cycles with minimal loss in capacity.[12,20]

The progression towards even higher nickel content in NCM ultimately leads to the end member of this family of materials, $LiNiO_2$ (LNO).[21] However, the synthesis of single-crystalline LNO (SC-LNO) is challenging and up to date, no such material has been presented that would be suitable for battery application.[21] Single-crystalline NCM materials are commonly prepared by a sintering technique at elevated temperatures to fuse smaller primary particles (crystallites) into larger, μm-sized crystallites.[22] The resulting "single-crystalline" materials, however, mostly still consist of agglomerated crystallites.[22] While Co and Mn stabilize the structure of NCM at these high sintering temperatures (>800 °C), LNO suffers from fast decomposition towards Li-deficient phases.[23,24] Consequently, SC-LNO shows a high off-stoichiometry (x in $Li_{1-x}Ni_{1+x}O_2$ hereafter), when synthesized with this sintering technique.[21,25] Even state-of-the-art polycrystalline LNO, which is calcined at around 700 °C shows values of x in the range of 1–2%, while stoichiometric LNO has yet to be demonstrated.[26,27] It has been shown that at a temperature of 720 °C coarse-grain LNO can be synthesized with a low x, but the primary particle size is still small and the degree of agglomeration too high for the successful application in SSBs.[28,29]

In this work, we use an alternative approach to prepare SC-LNO, consisting of μm-sized, well-separated crystals with $x < 2\%$. The idea is to produce the SC-LNO not by a high-temperature sintering process, but instead to use a flux-assisted approach to grow crystallites through an Ostwald ripening mechanism. For this, we use a Li_2CO_3 melt at only 750 °C that also provides a high chemical potential of Li_2O to further push the equilibrium towards a low x. We investigate the influence of annealing time and precursor particle size on the Li off-stoichiometry and the morphology of SC-LNO by X-ray diffraction (XRD) and scanning electron microscopy (SEM), respectively. Thereby, we identify synthesis conditions to grow well-separated SC-LNO with particle size and structural quality suitable for battery application. With this material, we demonstrate good

[z]E-mail: juergen.janek@phys.chemie.uni-giessen.de

performance in SSB cells with a high specific capacity of >200 mAh g^{-1} at 25 °C and C/20 rate and superior capacity retention over state-of-the-art polycrystalline LNO in liquid electrolyte LIBs.

Results and Discussion

To synthesize SC-LNO, we started by annealing a mixture of NiO and $LiOH{\cdot}H_2O$ (10 mol% excess) at 825 °C for 6 h followed by 680 °C for another 6 h. This procedure is referred to as 1st step in the following. The resulting material consisted of μm-sized, primary particles (crystallites) that were agglomerated into larger secondary particles as can be seen in Fig. 1a. To further grow and separate the crystallites, this powder was then mixed by hand grinding with 0.8 lithium equivalents (30 wt%) of Li_2CO_3, pressed into a pellet and annealed at 750 °C. The procedure is referred to as 2nd step hereafter. The Li_2CO_3 melts at around 720 °C, thus, the SC-LNO is then immersed into a melt and crystallites grow through Ostwald ripening. We note that sufficient grinding of the SC-LNO and Li_2CO_3 is decisive for the final particle size, as a high degree of agglomeration would cause significant sintering to form larger particles. After taking the mixture out of the oven, the pellet was still intact and could be easily removed from the crucible. We also tested higher amounts of Li_2CO_3, which eventually led to deliquescence of the pellet. The latter made it impossible to remove the pellet from the crucible. As the pellet still contains all of the Li_2CO_3, we hand mortared it into a fine powder and immersed it into water to dissolve the carbonate. A washing step is commonly also needed for Ni-rich NCM materials as they are typically synthesized with an excess of Li-precursor. [25,26,30] However, this step is more critical in the present case, as a large amount of water is required to dissolve the comparably large amount of excessive Li_2CO_3. Consequently, we consider the separation of the flux and SC-LNO as the most challenging step for a potential scale-up. Therefore, we washed around 1 g of LNO in 30 ml of ice-cooled water during vigorous agitation for 1 min, followed by centrifugation and discarding the supernatant fluid. This step was repeated twice. It should be noted that Li_2CO_3 has a higher solubility in cold water, while Li^+-leaching (Li^+/H^+ exchange) from LNO should be attenuated. By acid titration after the washing step we confirmed that the residual Li_2CO_3 in the final SC-LNO powder was around 2 wt%. The entire synthesis procedure is sketched in Scheme 1.

We also attempted a single-step synthesis using a mixture of NiO and Li_2CO_3 to circumvent the lithiation of NiO by LiOH and combine the two synthesis steps. However, XRD indicated that there were still large amounts of unreacted Li_2CO_3 and the LNO was highly Li-deficient even after 9 h of reaction at 825 °C (Fig. SI-1). We attribute this to the thermodynamically slower decomposition of Li_2CO_3 compared to LiOH, as discussed in detail in a previous report. [31] This shows that an initial lithiation from LiOH cannot be easily avoided and suggests the necessity of a two-step process.

SEM images of the resulting materials are shown in Figs. 1b—1d, where the 2nd step was performed for 3 h, 12 h or 40 h, respectively. Already after 3 h annealing in the Li_2CO_3 melt, the crystals were well separated and the size increased considerably. Particle size distributions of these materials are reported in Fig. SI-2. Hereby we note that CAMs consisting of μm-sized crystallites are often referred to as "single-crystalline" even if they are agglomerated into larger secondary particles.[22] For consistency with other literature and industry, we refer to the material as well-separated single crystals judging from the absence of significant grain boundaries in SEM. Longer annealing further increased the particle size and eventually induced an octahedral shape. Such shape has been previously reported for NCM crystals synthesized in a Li_2CO_3 melt.[32] In Figures 1e and 1f, the annealing at 750 °C was followed by annealing at somewhat lower temperature (680 °C), with the idea of exposing the LNO to a less reducing atmosphere while still enabling ion motion to push the equilibrium more towards stoichiometric LNO.[23] As can be seen, this lower temperature step had no significant effect on both particle size and shape.

Overall, the crystals grew to a large size after the 2nd step, which may be detrimental to the rate performance.[28] Therefore, we attempted to synthesize SC-LNO with smaller particle size by reducing the annealing temperature in the 1st step to 780 °C. As can be seen in Fig. 1g, this resulted in significantly smaller primary crystals. This material was also subjected to the 2nd step in the Li_2CO_3 melt for 3 h at 750 °C (Fig. 1h) or 40 h at 750 °C followed by 20 h at 680 °C (Fig. 1i). The particle size of the SC-LNO after the 2nd step was also significantly reduced as compared to the materials discussed above. The average particle diameter (D_{50}) was around 3.4 μm, which is consistent with that of other single-crystalline NCM CAMs. From a morphological point of view, the materials shown in Figs. 1h and 1i can be considered suitable for application in batteries. In the following, we will refer to these small-particle materials as *SC-LNO SP3* and *SC-LNO SP40–20*, respectively.

In addition to the morphological characterization by SEM, we determined the structure of the synthesized SC-LNO powders by XRD and performed Rietveld refinements to fit the $Li_{1-x}Ni_{1+x}O_2$ structure to the data. The XRD patterns and respective fits can be found in Fig. SI-3 and the detailed results from the refinements in Table SI-1. To assess the structural quality, we show the refined off-stoichiometry x in $Li_{1-x}Ni_{1+x}O_2$ in Fig. 2a. After the 1st synthesis step at 825 °C, x is comparably high with around 3.5%. Since a high amount of Ni^{2+} on the Li^+ site is adverse to the transport of Li^+, a low x has to be targeted.[33] As the 2nd synthesis step is performed in a Li_2CO_3 melt, the high chemical potential of Li_2O drives the reaction towards lower x. In fact, we observed a continuous decrease in x upon longer annealing at 750 °C in the Li_2CO_3 melt and further upon annealing at 680 °C. When the 1st step is carried out at only 780 °C the initial x is found to be significantly lower as compared to the material annealed at 825 °C. Consequently, after 40 h at 750 °C and 20 h at 680 °C, the *SC-LNO SP40–20* reaches $x \approx 1.8\%$.

In order to benchmark our results with previous reports, we compared the refined unit cell volumes V_{cell} and corresponding x with the data presented by Kurzhals et al. (Fig. 2b).[26] It is important to note that especially the off-stoichiometry is susceptible to systematic errors from the experimental side (e.g., XRD sample preparation, preferential orientations etc.) and from the refinement side as it correlates in effect with other parameters (e.g., choice of temperature factors). V_{cell} can be considered a more robust parameter that, among other effects, reflects also changes in stoichiometry. Therefore, such an alignment with literature data would confirm the validity of the presented results. In fact, the V_{cell} and x obtained from our refinements align well with the data from Kurzhals et al.[26] We also included the results for state-of-the-art polycrystalline LNO (PC-LNO), which shows an $x \approx 1.3\%$ with approximately the same V_{cell} as our *SC-LNO SP40–20* sample. This suggests that both materials are comparable in terms of structure and defects.

SSB cells with *SC-LNO SP3* and *SC-LNO SP40–20* as CAM were prepared to test the electrochemical performance and compared to the state-of-the-art PC-LNO. The cell setup is sketched in the inset in Fig. 3a. A cross-sectional SEM image of the cathode using *SC-LNO SP40–20* is shown in Figs. SI-4, which highlights the good separation of the individual SC-LNO crystals. We used Li_3InCl_6 as solid electrolyte (SE) in the cathode because of its high stability against electrochemical oxidation at potentials up to around 3.7 V vs. In/InLi.[34,35] To ensure complete ionic percolation, we use excess amounts of Li_3InCl_6 in the cathode (36 wt%) which is far more than used in high energy-density cathodes and results in the presence of larger agglomerations of Li_3InCl_6 as can be seen in Fig. SI-4. The use of Li_3InCl_6 allows us to ameliorate the impact of interfacial degradation in the cathode and shift the focus of the discussion on the morphological and structural properties of LNO. As the LNO materials employed in this work were not coated by a protective layer, this would otherwise lead to rapid performance degradation if the more conventional thiophosphate-based solid electrolytes were used.[29] Nonetheless, at the In/InLi anode (~0.62 V vs Li^+/Li) we used Li_6PS_5Cl, because Li_3InCl_6 has the tendency to form a highly

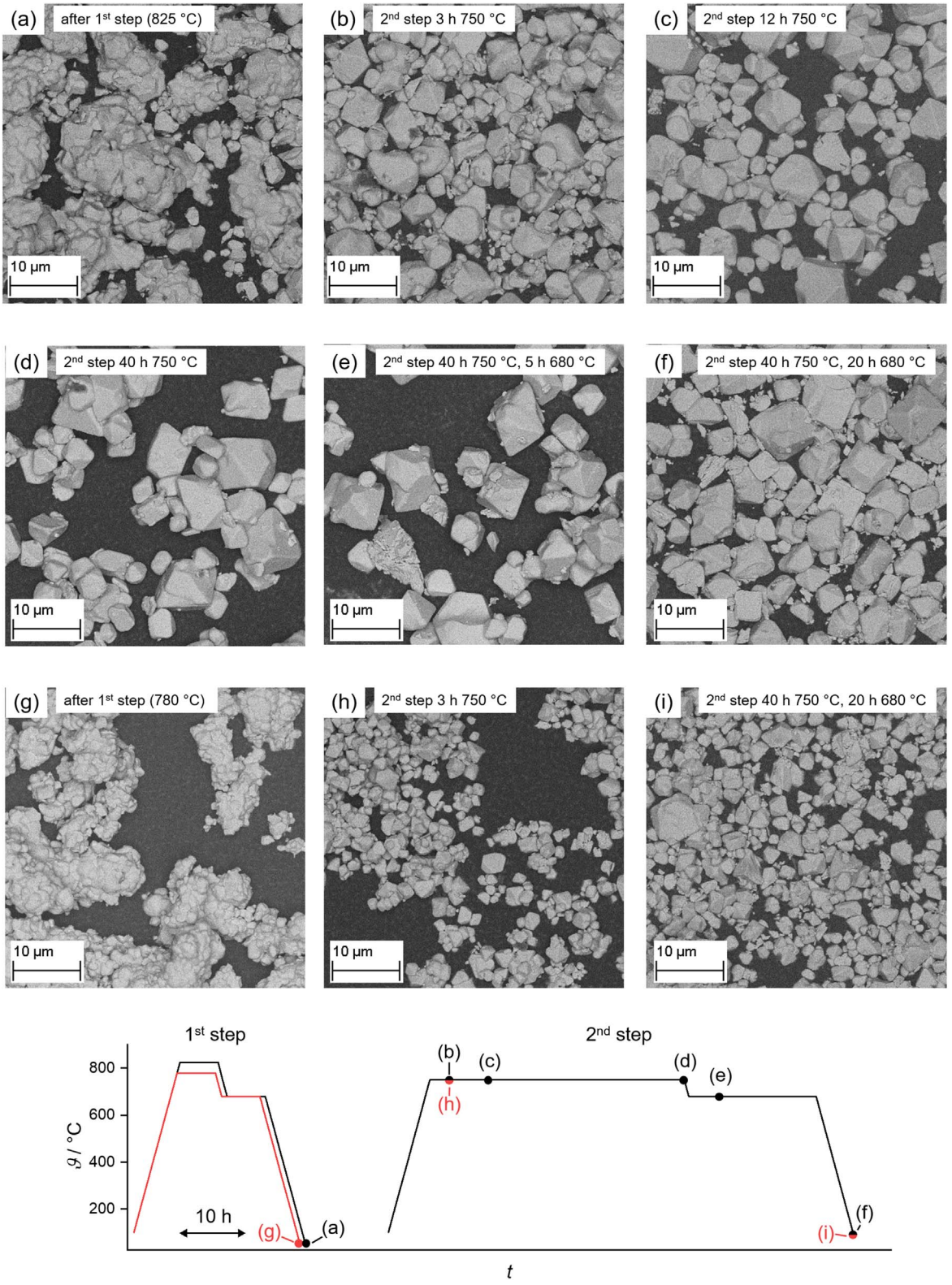

Figure 1. SEM images of SC-LNO after the 1st synthesis step with annealing temperature of (a) 825 °C and after the 2nd step in a Li_2CO_3 melt at 750 °C for (b) 3 h, (c) 12 h and (d—f) 40 h. The SC-LNO CAMs shown in (e) and (f) have been held at 680 °C for 5 h and 20 h, respectively, subsequent to the 750 °C step. (g) SC-LNO after the 1st step at only 780 °C that was then annealed in a Li_2CO_3 melt at 750 °C for (h) 3 h or (i) 40 h and 680 °C for 20 h. A temperature-vs-time-plot (ϑ vs t) is shown at the bottom indicating at which stage of the synthesis the different SEM images were taken.

resistive interphase upon reduction at the negative electrode side, which would be detrimental to the cell performance.[36]

The first cycles at 25 °C with a charging and discharging current of C/20 (1 C = 200 mA g^{-1}) are shown in Fig. 3a as solid lines. *SC-LNO SP40–20* delivered the highest specific discharge capacity (q_{dis}) of 203 mAh g^{-1} with a first-cycle Coulomb efficiency (*CE*) of 85.1%, followed by *SC-LNO SP3* with q_{dis} = 188 mAh g^{-1} and *CE* = 82.4%. PC-LNO performed worst with q_{dis} = 154 mAh g^{-1} and

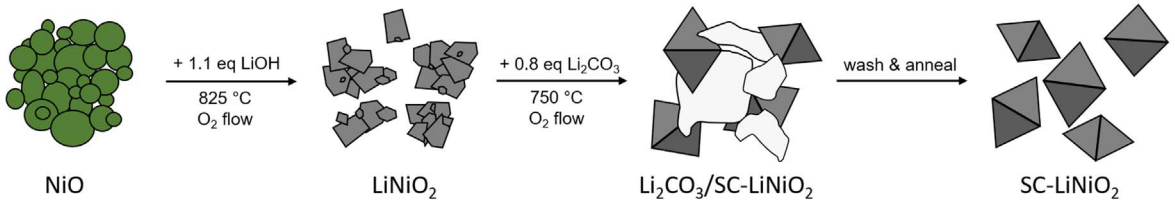

Scheme 1. Schematic representation of the synthesis protocol from NiO towards SC-LNO.

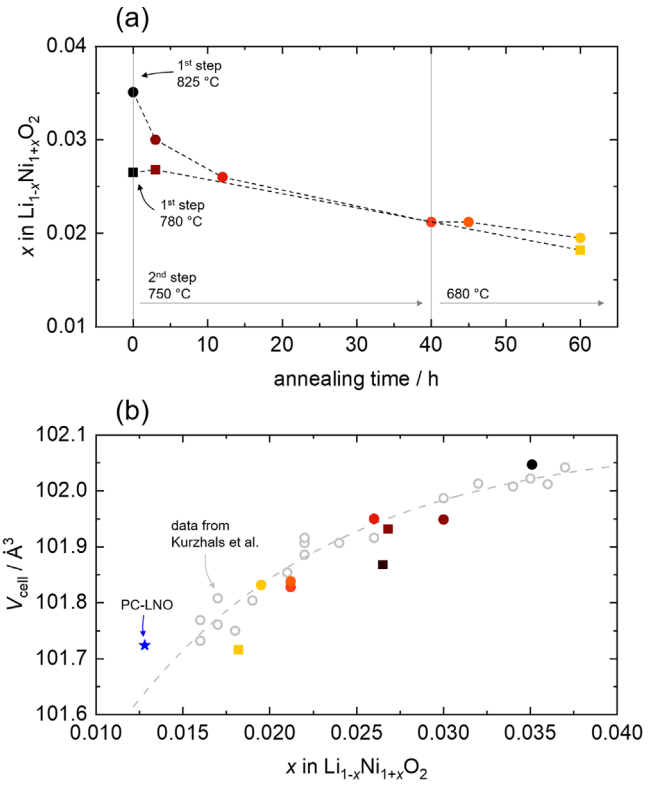

Figure 2. (a) Off-stoichiometry x in $Li_{1-x}Ni_{1+x}O_2$ from Rietveld refinement analysis for the SC-LNO materials after the 1st synthesis step (black symbols) and the corresponding materials after the 2nd synthesis step (colored symbols). (b) Unit cell volumes V_{cell} and off-stoichiometry x shown together with the data reported by Kurzhals et al.[26]

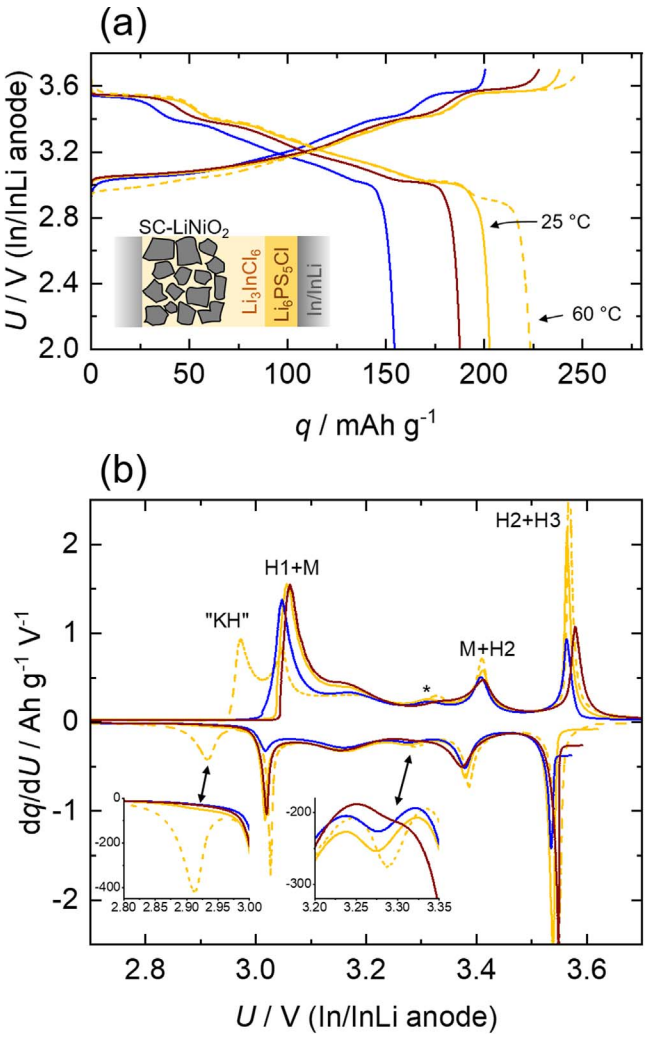

Figure 3. (a) First cycle charge-discharge curves at 25 °C and C/20 rate of SSBs with PC-LNO (blue), *SC-LNO SP3* (red) and *SC-LNO SP40–20* (yellow) and at 60 °C and C/10 rate for *SC-LNO SP40–20* (yellow dashed). A sketch of the SSB cell is shown in the inset. (b) Differential capacity plots of the cells shown above.

$CE = 77.0\%$. In agreement with previous literature on SSBs, large particles suffer from significant kinetic limitations even at a low C-rate of C/20.[4,6] Such kinetic limitations can be lifted by an increased temperature. In fact, a cell with *SC-LNO SP40–20* cycled at 60 °C and C/10 rate delivered $q_{dis} = 223$ mAh g^{-1}, with the most significant gain in an additional voltage-plateau around 2.9 V. This plateau and the limitations are discussed below in some more detail. In view of these kinetic limitations, small particle SC-LNO materials should achieve significantly higher q_{dis} and CE. However, in the present case we observed a lower capacity for *SC-LNO SP3* even though the particle size is smaller than that of *SC-LNO SP40–20*.

To investigate the reason behind this, we looked at the differential capacities dq/dU (Fig. 3b). For all materials, distinct peaks corresponding to the expected two-phase coexistence regions (H1 + M, M + H2 and H2 + H3) can be seen.[37,38] Upon closer inspection of the H2 + H3 peaks, however, one can see that this transition appears to be shifted to higher voltages for the *SC-LNO SP3* material, while it occurs at approximately the same voltages for *SC-LNO SP40–20* and PC-LNO at 25 °C. Such shift in potential of the H2 + H3 transition has been discussed in detail in previous literature reports.[26] In short, its average potential depends on the off-stoichiometry x, with higher x resulting in an increased voltage required to initiate the phase transition. Furthermore, the peak in dq/dU at ~3.3 V (marked with an asterisk and magnified in the inset in Fig. 3b), which corresponds to a transition between two ordered lithium sub-structures, also serves as a signature of a low degree of defects.[26] It is evident that this peak is present to a similar extent for *SC-LNO SP40–20* and PC-LNO at 25 °C, whereas it is clearly suppressed for *SC-LNO SP3*. These observations further corroborate the results from XRD, that *SC-LNO SP40–20* and PC-LNO are basically equivalent in terms of structural quality, while *SC-LNO SP3* shows a larger x.

As has been shown in literature, x significantly impairs the Li^+ diffusion inside the LNO as the Ni^{2+} on the Li^+ site not only blocks one single site, but also anchors surrounding Li^+ in place.[33,38,39]

Therefore, it can be expected that the capacity of *SC-LNO SP3* is even more affected by kinetic limitations, despite the more favorable particle size. In fact, when taking a closer look at the dq/dU at low voltages (inset in Fig. 3b), one can see a shoulder for *SC-LNO SP40–20* at ∼2.9 V even when cycled at 25 °C, which becomes very significant at 60 °C but is absent for the other two materials. This region in the dq/dU data is commonly referred to as "kinetic hindrance" ("KH") region, as the high degree of lithiation and low vacancy concentration lead to very slow Li^+ transport.[37] A low dq/dU in the "KH" region indicates more severe kinetic limitations.[40] Thus, structural imperfections become apparent here, which clearly underlines the importance of both particle size and off-stoichiometry for the performance of LNO in SSBs.

The kinetic limitation of the capacity of *SC-LNO SP40–20* further becomes apparent when compared to PC-LNO in liquid-electrolyte-based LIBs (Fig. 4a). PC-LNO achieved a q_{dis} = 230 mAh g^{-1} at 25 °C and C/20, whereas *SC-LNO SP40–20* only delivered 209 mAh g^{-1}. Obviously, the additional capacity of PC-LNO mostly stems from the "KH" plateau at the low voltage end of the discharge, whereas the other parts of the capacity-voltage-profiles overlap. Notably, the capacity of *SC-LNO SP40–20* in the SSB is almost the same as for the liquid-electrolyte-based LIB, with only a minor gap that probably originates from non-ideal electronic or ionic percolation. Overall, we conclude that *SC-LNO SP40–20* in the presented SSBs is close to reaching the highest achievable capacity that can be achieved for single-crystalline LNO particles of this size.

Furthermore, when comparing the long-term cycling performance of *SC-LNO SP40–20* in SSBs and liquid-electrolyte-based LIBs (Fig. 4b), we find remarkably overlapping behavior of both for 150 cycles at 25 °C and C/2 rate. This suggests that the main reason for the capacity fading is not caused by the electrolyte, but is rather an intrinsic problem of LNO, such as the structural instability at high degrees of delithiation. This has been the subject of previous studies and a further detailed investigation on the root causes of the capacity fading is beyond the scope of this work.[21] However, it can clearly be seen that the fading for PC-LNO in liquid electrolyte LIBs is progressing at a faster rate than for the cells with *SC-LNO SP40–20*. Although PC-LNO delivers initially higher specific capacities, the faster fading eventually leads to a lower capacity after around 100 cycles. The differences in fading rate between PC-LNO and *SC-LNO SP40–20* could be ascribed to the improved morphological stability of SC-LNO. In addition, as the lower specific capacities of SC-LNO in comparison to PC-LNO are resulting from the kinetic limitation, cycling at elevated temperature is able to significantly improve the performance of SC-LNO in SSBs (Fig. 4c). For this experiment we used a lithium titanate (LTO) anode without excess lithium and are able to demonstrate a stable cycling performance with q_{dis} = 155 mAh g^{-1} at C/2 rate and q_{dis} = 200 mAh g^{-1} at C/20 rate after 100 cycles at 45 °C. This shows that *SC-LNO SP40–20* can deliver and maintain a high performance during cycling even in SSB full cells.

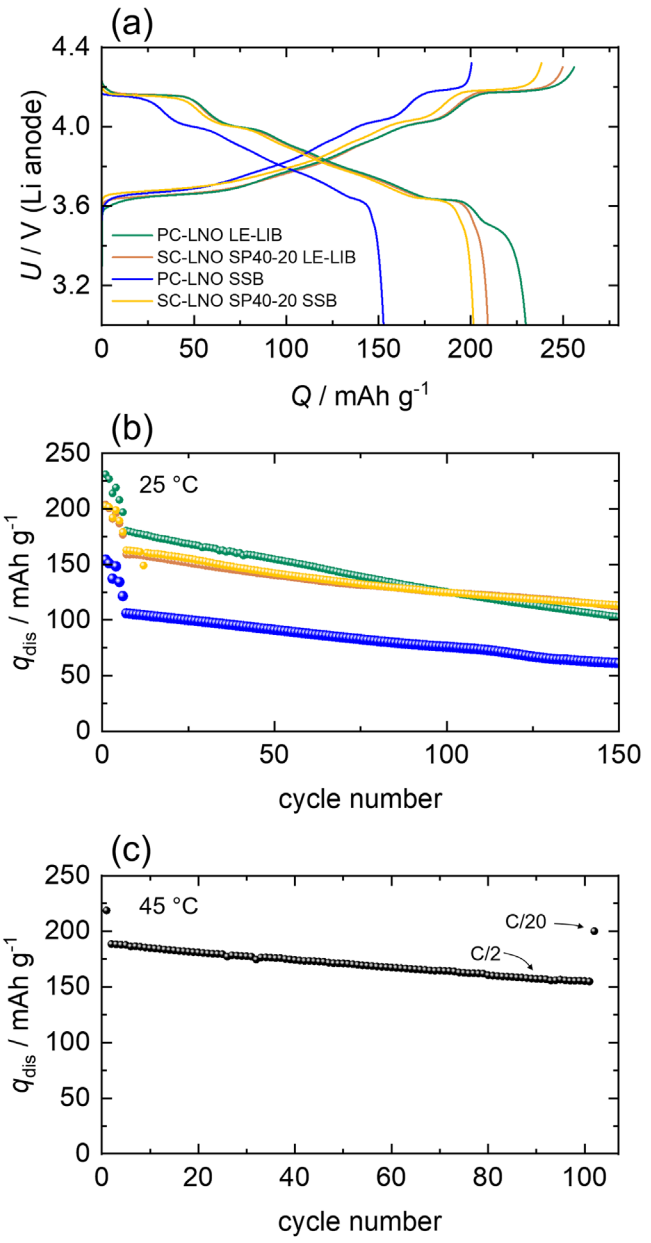

Figure 4. (a) First-cycle charge-discharge curves at 25 °C and C/20 rate of SSBs with PC-LNO (blue) and *SC-LNO SP40–20* (yellow) and the corresponding liquid-electrolyte-based LIBs (LE-LIBs) in green and orange, respectively. The voltage of the SSBs was scaled to the Li-metal anode employed in the LE-LIBs by adding 0.62 V. (b) Evolution of the specific discharge capacity q_{dis} of the respective cells during continuous cycling at 25 °C. The C-rate for the long-term cycling was set to C/2. (c) q_{dis} of a SSB with *SC-LNO SP40–20* as cathode and LTO as anode active materials during continuous cycling at 45 °C. The C-rate for the long-term cycling was set to C/2, while the initial and last cycles were performed at C/20.

Methods

Synthesis of SC-LNO.—For the 1st step in the synthesis of SC-LNO, 1.1 molar equivalents of $LiOH{\cdot}H_2O$ (Sigma-Aldrich) were hand ground in a mortar for 8 min, followed by adding 1 molar equivalent of NiO (325 mesh, Alfa Aesar) and grinding for another 7 min. The mixture was then loaded into alumina crucibles and annealed under oxygen flow (100 cm^3 min^{-1}) at 825 °C or 780 °C for 6 h followed by annealing at 680 °C for 6 h. Heating and cooling ramps were both set at 100 °C min^{-1}. After cooling, the black brick-like material was ground into a fine powder for 15 min and stored in an Ar-filled glovebox until further use.

For the 2nd synthesis step of SC-LNO, the above powder was mixed with 0.4 molar equivalents of Li_2CO_3 (Alfa Aesar) by hand grinding for 5 min. This mixture was then pressed at 100 MPa and the pellets were loaded into alumina crucibles and annealed as specified in the main text. After cooling, the pellets were crushed in a mortar until a fine powder was obtained. This powder was then dispersed in ice-cooled MilliQ-water (1 g LNO per 30 ml water) and vigorously agitated for 1 min. Immediately afterwards, the mixture was centrifuged (4000 rpm for 2 min) and the supernatant water was discarded. The washing procedure was repeated two more times. Subsequently, the powder was washed in ethanol and acetone, followed by post-annealing at 700 °C for 3 h under oxygen flow (100 cm^3 min^{-1}). Finally, the powder was ground for 3 min, sieved (45 μm mesh size), vacuum-dried at 200 °C overnight and stored in an Ar-filled glovebox until further use.

Scanning electron microscopy.—SEM was performed on the synthesized powders by dispersing them onto adhesive carbon tape and transferring them into a ZEISS Merlin FE-SEM. The samples were probed with a 1 nA current at 7 kV voltage and the back-scattered electrons were detected.

X-ray diffraction and structural refinement.—XRD was performed on LNO powders filled into glass capillaries with 0.5 mm inner diameter. The samples were mounted in an Empyrean 3 diffractometer (Malvern PANalytical) with Mo-Kα source and measured in Debye–Scherrer geometry. The angular 2Θ range was 5°–40° with a step size of 0.007° and a scan speed of 1° min^{-1}.

A $Li_{1-x}Ni_{1+x}O_2$ structure (space group R $\bar{3}$ m) was refined with a pseudo-Voigt profile by using the software Fullprof to match the measured pattern. The instrumental parameters (U, V, W, X, Y) were determined beforehand by using a LaB_6 standard (NIST 660c). The refinement included the following parameters: 5 coefficients for the polynomial background; lattice parameters *a*, *b* and *c*; profile parameters *U*, *IG*, *X*, *Y*; asymmetry parameters *Asy1* and *Asy2*; site-occupancy *x* of Ni on Li-site; oxygen *z*-axis parameter; site-dependent temperature factors B_{iso}.

Electrochemical testing.—SSB cells were prepared inside an Ar-filled glovebox in a press-cell-type setup as described in detail elsewhere.[41] The cathode composite consisted of 63 wt% LNO, 36 wt% Li_3InCl_6 (NEI Corp.) and 1 wt% carbon fibers (Aldrich), which were mixed by hand grinding for 15 min. The cathode composite (4 mg cm^{-2} active material loading) was loaded onto a two-sided pelletized separator consisting of 50 mg Li_3InCl_6 (towards the cathode side) and 30 mg Li_6PS_5Cl (NEI Corp.) (towards the anode side). The cathode and separator were consolidated by pressing at 400 MPa. Afterwards, the anode was prepared by sequentially placing an indium foil (100 μm, ChemPur) and a lithium foil (100 μm, China Energy Lithium) on top of the separator. For SSB cells with LTO as anode, anode composites were prepared by milling 60 wt% Li_6PS_5Cl, 30 wt% carbon-coated LTO (NEI Corp.) and 10 wt% Super C65 (TIMCAL) using 10 zirconia balls with diameter 1 cm in a 70 ml planetary mill at 140 rpm for 30 min. The anode composite was placed on top of the separator and pressed in the same way as the cathode composite. The cell was then tightly sealed, taken out of the glovebox and a pressure of 120 MPa was applied, which was maintained throughout the experiments.

Liquid-electrolyte-based LIB cells were prepared inside an Ar-filled glovebox in a coin-cell-type setup. The cathode (3 mg cm^{-2} active material loading) was cast onto Al-foil from a slurry consisting of 90 wt% LNO, 5 wt% Super-P carbon (TIMCAL) and 5 wt% PVDF binder (Pi-KEM), the latter of which was dispersed in N-methyl^{-2}-pyrrolidone (NMP). The cathode-coated Al-sheet was vacuum-dried at 120 °C overnight and pressed at 100 MPa. The coin cells were assembled by sequentially adding the Al-clad cathode case (Pi-KEM), the cathode sheet, a polymer separator (Celgard), 80 μl electrolyte (LP-57, Sigma-Aldrich), a glass-fiber separator (GF/D, Whatman), a lithium chip (0.5 mm, Pi-KEM), stainless steel spring and spacer (Pi-KEM) and the stainless steel anode case (Pi-KEM). The cell stack was pressed and sealed inside a coin-cell crimper and transferred out of the glovebox for electrochemical experiments.

Electrochemical cell testing was performed by galvanostatic cycling on a series 4000 battery cycler (Maccor). Charging and discharging was performed at 25 °C with the same C-rate (1 C = 200 mA g^{-1}), which was C/20 (1st and 2nd cycles), C/10 (3rd cycle), C/20 (4th cycle), C/10 (5th cycle), C/5 (6th cycle) and C/2 for all following cycles. Cells cycled at 45 °C with LTO as anode were charged and discharged at C/20 rate (1st and 102nd cycles) and C/2 rate for all other cycles. The initial charging and discharging cycles were carried out at least on two identical cells for each LNO tested, whereas the specific capacities of these cells deviated by less than 5% from each other.

Conclusions

In this work, we presented a synthesis route for single-crystalline LNO powders with high structural and morphological quality for application in high-capacity SSBs. The key idea is to subject agglomerated LNO crystallites to a Li_2CO_3 melt that leads to growth and separation of primary particles and further provides a high chemical potential of Li_2O to prevent and reverse lithium loss. With this method, it was possible to synthesize SC-LNO with a particle size of $D_{50} \approx 3.4$ μm and an off-stoichiometry of $x < 2\%$. In SSB cells, this material delivered a specific discharge capacity $q_{dis} = 203$ mAh g^{-1} at 25 °C and C/20 rate and outperformed state-of-the-art polycrystalline LNO. Upon long-term cycling, the single-crystalline morphology was found attenuate capacity fading and deliver a stable and high performance in SSB full cells at elevated temperature.

Acknowledgments

Financial support by BASF SE and by BMBF (Bundesministerium für Bildung und Forschung, Germany) within the cluster of competence FESTBATT (projects 03XP0177A and 03XP0430A) and EProFest (03XP0346D) is gratefully acknowledged.

ORCID

Raffael Rueß https://orcid.org/0000-0002-9274-4714
Enrico Trevisanello https://orcid.org/0000-0001-7482-9418
Yuan Ma https://orcid.org/0000-0003-4369-9520
Torsten Brezesinski https://orcid.org/0000-0002-4336-263X
Jürgen Janek https://orcid.org/0000-0002-9221-4756

References

1. L. Kong, L. Wang, J. Zhu, J. Bian, W. Xia, R. Zhao, H. Lin, and Y. Zhao, *Chem. Commun.*, **57**, 12587 (2021).
2. J. Janek and W. G. Zeier, *Nat. Energy*, **1**, 1167 (2016).
3. F. Strauss, T. Bartsch, L. de Biasi, A.-Y. Kim, J. Janek, P. Hartmann, and T. Brezesinski, *ACS Energy Lett.*, **3**, 992 (2018).
4. R. Ruess, S. Schweidler, H. Hemmelmann, G. Conforto, A. Bielefeld, D. A. Weber, J. Sann, M. T. Elm, and J. Janek, *J. Electrochem. Soc.*, **167**, 100532 (2020).
5. S. Payandeh, D. Goonetilleke, M. Bianchini, J. Janek, and T. Brezesinski, *Curr. Opin. Electrochem.*, **31**, 100877 (2022).
6. Y. Han, S. H. Jung, H. Kwak, S. Jun, H. H. Kwak, J. H. Lee, S.-T. Hong, and Y. S. Jung, *Adv. Energy Mater.*, **22**, 2100126 (2021).
7. X. Liu et al., *Adv. Energy Mater.*, **11**, 2003583 (2021).
8. C. Doerrer, I. Capone, S. Narayanan, J. Liu, C. R. M. Grovenor, M. Pasta, and P. S. Grant, *ACS Appl. Mater. Inter.*, **13**, 37809 (2021).
9. N. Sun et al., *Adv. Energy Mater.*, **2200682** (2022).
10. G. Conforto, R. Ruess, D. Schröder, E. Trevisanello, R. Fantin, F. H. Richter, and J. Janek, *J. Electrochem. Soc.*, **168**, 70546 (2021).
11. W. Zhao et al., *Small*, **18**, e2107357 (2022).
12. J. E. Harlow et al., *J. Electrochem. Soc.*, **166**, A3031 (2019).
13. H. Li, A. Liu, N. Zhang, Y. Wang, S. Yin, H. Wu, and J. R. Dahn, *Chem. Mater.*, **31**, 7574 (2019).
14. X. Fan, G. Hu, B. Zhang, X. Ou, J. Zhang, W. Zhao, H. Jia, L. Zou, P. Li, and Y. Yang, *Nano Energy*, **70**, 104450 (2020).
15. F. Strauss, J. H. Teo, A. Schiele, T. Bartsch, T. Hatsukade, P. Hartmann, J. Janek, and T. Brezesinski, *ACS Appl. Mater. Inter.*, **12**, 20462 (2020).
16. S. Oswald, M. Bock, and H. A. Gasteiger, *J. Electrochem. Soc.*, **169**, 50501 (2022).
17. B. Strehle, F. Friedrich, and H. A. Gasteiger, *J. Electrochem. Soc.*, **168**, 50512 (2021).
18. A. O. Kondrakov, A. Schmidt, J. Xu, H. Geßwein, R. Mönig, P. Hartmann, H. Sommer, T. Brezesinski, and J. Janek, *J. Phys. Chem. C*, **121**, 3286 (2017).
19. S. Klein, P. Bärmann, O. Fromm, K. Borzutzki, J. Reiter, Q. Fan, M. Winter, T. Placke, and J. Kasnatscheew, *J. Mater. Chem. A*, **9**, 7546 (2021).
20. C. P. Aiken, E. R. Logan, A. Eldesoky, H. Hebecker, J. M. Oxner, J. E. Harlow, M. Metzger, and J. R. Dahn, *J. Electrochem. Soc.*, **169**, 50512 (2022).
21. M. Bianchini, M. Roca-Ayats, P. Hartmann, T. Brezesinski, and J. Janek, *Angew. Chem. Int. Ed.*, **58**, 10434 (2019).
22. J. Langdon and A. Manthiram, *Energy Storage Mater.*, **37**, 143 (2021).
23. M. Bianchini, F. Fauth, P. Hartmann, T. Brezesinski, and J. Janek, *J. Mater. Chem. A*, **8**, 1808 (2020).
24. K. Ryu, M. A. Abbas, and J. H. Bang, *ACS Energy Lett.*, **7**, 2029 (2022).
25. A. Liu, N. Zhang, J. E. Stark, P. Arab, H. Li, and J. R. Dahn, *J. Electrochem. Soc.*, **168**, 40531 (2021).
26. P. Kurzhals, F. Riewald, M. Bianchini, H. Sommer, H. A. Gasteiger, and J. Janek, *J. Electrochem. Soc.*, **168**, 110518 (2021).
27. A. Mesnier and A. Manthiram, *ACS Appl. Mater. Inter.*, **12**, 52826 (2020).

28. F. Riewald, P. Kurzhals, M. Bianchini, H. Sommer, J. Janek, and H. A. Gasteiger, *J. Electrochem. Soc.*, **169**, 20529 (2022).
29. Y. Ma, J. H. Teo, D. Kitsche, T. Diemant, F. Strauss, Y. Ma, D. Goonetilleke, J. Janek, M. Bianchini, and T. Brezesinski, *ACS Energy Lett.*, **6**, 3020 (2021).
30. D. Pritzl, T. Teufl, A. T. S. Freiberg, B. Strehle, J. Sicklinger, H. Sommer, P. Hartmann, and H. A. Gasteiger, *J. Electrochem. Soc.*, **166**, A4056 (2019).
31. R. Ruess, M. A. Ulherr, E. Trevisanello, S. Schröder, A. Henss, and J. Janek, *J. Electrochem. Soc.*, **169**, 70531 (2022).
32. J. Zhu and G. Chen, *J. Mater. Chem. A*, **7**, 5463 (2019).
33. N. Phattharasupakun, M. M. E. Cormier, E. Lyle, E. Zsoldos, A. Liu, C. Geng, Y. Liu, H. Li, M. Sawangphruk, and J. R. Dahn, *J. Electrochem. Soc.*, **168**, 90535 (2021).
34. X. Li, J. Liang, X. Yang, K. R. Adair, C. Wang, F. Zhao, and X. Sun, *Energy Environ. Sci.*, **13**, 1429 (2020).
35. L. Nazar, I. Kochetkov, T.-T. Zuo, R. Ruess, B. Singh, L. Zhou, K. Kaup, and J. Janek, *Energy Environ. Sci.* (2022).
36. L. M. Riegger, R. Schlem, J. Sann, W. G. Zeier, and J. Janek, *Angew. Chem. Int. Ed.*, **60**, 6718 (2021).
37. H. Li, N. Zhang, J. Li, and J. R. Dahn, *J. Electrochem. Soc.*, **165**, A2985 (2018).
38. M. Mock, M. Bianchini, F. Fauth, K. Albe, and S. Sicolo, *J. Mater. Chem. A*, **9**, 14928 (2021).
39. C. Delmas, J. P. Pérès, A. Rougier, A. Demourgues, F. Weill, A. Chadwick, M. Broussely, F. Perton, P. Biensan, and P. Willmann, *J. Power Sources*, **68**, 120 (1997).
40. A. Liu, N. Phattharasupakun, M. M. E. Cormier, E. Zsoldos, N. Zhang, E. Lyle, P. Arab, M. Sawangphruk, and J. R. Dahn, *J. Electrochem. Soc.*, **168**, 70503 (2021).
41. W. Zhang et al., *ACS Appl. Mater. Inter.*, **9**, 17835 (2017).